Electric-Field-Tunable Valley Zeeman Effect in Bilayer Graphene Heterostructures: Realization of the Spin-Orbit Valve Effect

Priya Tiwari, Saurabh Kumar Srivastav⬛, and Aveek Bid⬛[*]

Department of Physics, Indian Institute of Science, Bangalore 560012, India

We report the discovery of electric-field-induced transition from a topologically trivial to a topologically nontrivial band structure in an atomically sharp heterostructure of bilayer graphene (BLG) and single-layer WSe_2 per the theoretical predictions of Gmitra and Fabian [Phys. Rev. Lett. **119,** 146401 (2017)]. Through detailed studies of the quantum correction to the conductance in the BLG, we establish that the band-structure evolution arises from an interplay between proximity-induced strong spin-orbit interaction (SOI) and the layer polarizability in BLG. The low-energy carriers in the BLG experience an effective valley Zeeman SOI that is completely gate tunable to the extent that it can be switched on or off by applying a transverse displacement field or can be controllably transferred between the valence and the conduction band. We demonstrate that this results in the evolution from weak localization to weak antilocalization at a constant electronic density as the net displacement field is tuned from a positive to a negative value with a concomitant SOI-induced splitting of the low-energy bands of the BLG near the $K(K')$ valley, which is a unique signature of the theoretically predicted spin-orbit valve effect. Our analysis shows that quantum correction to the Drude conductance in Dirac materials with strong induced SOI can only be explained satisfactorily by a theory that accounts for the SOI-induced spin splitting of the BLG low-energy bands. Our results demonstrate the potential for achieving highly tunable devices based on the valley Zeeman effect in dual-gated two-dimensional materials.

Over the past decade, the search for new quantum materials has attracted much interest from physicists and material scientists. A route to engineer new materials with a desirable set of properties is via van der Waals hetero-structures of two-dimensional (2D) materials [1–7]. This has led to the emergence of materials with designer properties not present in the parent components. For example, there is a particular interest in gaining the ability to manipulate the spin degree of freedom in graphene electrically. The intrinsic spin-orbit interaction (SOI) in graphene being very small (10 μeV) [8], this endeavor has met with minimal success. Several efforts have been made to increase the SOI in graphene, including doping it with the heavy atoms [9] or topological nanoparticles [10]; this has been achieved at the cost of degrading the quality of graphene.

Recently, both theoretical [11–15] and experimental [16–22] studies have indicated that strong SOI can be "induced" in graphene when placed on ultrathin films of transition metal dichalcogenides (TMD). Broken inversion symmetry, coupled with the presence of heavy atoms, leads to the appearance of strong intrinsic Ising spin-orbit coupling in single-layer TMD [11,12]. When placed in close proximity to graphene, the hybridization of d orbitals of the TMD with those of carbon in graphene leads to the appearance of a large SOI in the latter. The case of bilayer graphene (BLG) is particularly interesting: As the SOI is induced by a modification of the band structure of BLG, it opens up an avenue for preparing materials imbibing strong spin-polarizing SOI along with other desirable properties of BLG like high mobility, gate-tunable band gap, valley or layer polarizability for possible spintronics, and optoelectronics applications [23].

This proximity-induced SOI in the low-energy bands of BLG has two primary components—a valley Zeeman term that causes spin splitting of the band structure and a Kane-Mele term that opens up a topological gap at the two nonequivalent valleys, $\pm K$ [11,12,18,23,24]. It was predicted that for BLG on a single layer of WSe_2, the strength of the SOI in the valence band (VB) of the BLG ($\sim$2 meV) could be 2 orders of magnitude larger than that in the conduction band (CB) [11]. This is because the VB is formed by the nondimer carbon atom orbitals in the BLG bottom layer, which are in proximity with WSe_2. In contrast, the CB is formed by the nondimer orbitals of the top layer of the BLG, where the SOI strength remains similar to that in intrinsic BLG [11,25]. The induced SOI is manifested as a relatively large, spin-polarized splitting of the VB of the BLG.

Further, by applying an electric field of sufficient strength perpendicular to the interface, it is possible to invert the band structure, i.e., close the band gap and reopen

it—but this time transferring the SOI-induced splitting to the conduction band. Calculations show that by tuning the electric field, it is thus possible to transform the band structure of the BLG system from a topologically trivial to nontrivial. In recent work, we have demonstrated that this leads to the appearance of the time-reversal invariant $\mathbb{Z}_2$ topological phase in BLG [26]. Although SOI-induced splitting of the VB or CB was experimentally verified recently using penetration field capacitance measurements [17], direct transport observation of electric-field-induced band inversion is missing.

In this Letter, we present results of magnetotransport measurements in dual-gated h-BN/BLG/single-layer WSe$_2$/h-BN heterostructures explicitly designed to explore the proposal of Gmitra and Fabian [11]. We show a precise electric field tuning of the band-structure topology of BLG —from a doubly split CB and an unsplit VB at $D > 0$ to a doubly split VB and an unsplit CB at $D < 0$. Thus, the band-structure splitting could be controllably transferred from the VB to the CB using the electric field as an external tuning parameter. In a given band, the strength of the SOI was tunable by the electric field from a significant value to negligibly small, thus realizing the spin-orbit valve [11].

We further establish that the conventional McCann-Fal'ko equation [27], which has been used almost universally to study weak localization (WL) or weak antilocalization (WAL) in graphene or TMD heterostructures, is not appropriate to quantify the weak localization physics when there is a SOI-induced spin splitting of bands, as in our case. Instead, we show that the models developed by Ilić et al. [24] and Ochoa et al. [28] can account for the scattering mechanisms of the spin-split bands. We found that in the WAL case, the relevant parameters determining magnetotransport are the phase coherence time τ_ϕ and the antisymmetric spin relaxation τ_{asy} (which breaks the $z \to -z$ inversion symmetry). On the other hand, in the WL regime where the induced SOI is very small, the relevant timescales are τ_ϕ and intervalley scattering time τ_{iv}.

Heterostructures of h-BN/BLG/single-layer WSe$_2$/h-BN were fabricated using standard dry transfer technique [29,30] (see Supplemental Material [31]). Single-layer WSe$_2$ was used as it induces a much stronger SOI in BLG than thicker flakes. Figure 1(a) is the schematic showing the dual-gated architecture of the devices. Figure 1(b) is optical images of a device without top gate. All electrical measurements were performed at $T = 20$ mK in a dilution refrigerator unless specified, using standard low-frequency ac lock-in techniques.

The presence of both top and bottom gates in the device allowed independent tuning of n and D via the relations $n = [(C_{tg}V_{tg} + C_{bg}V_{bg})/e] - n_0$ and $D = [(C_{tg}V_{tg} - C_{bg}V_{bg})/2\epsilon_o] - D_0$. Here, n_0 is the residual charge density due to doping and D_0 is net internal displacement field. Figure 1(c) shows variation of the four-probe longitudinal resistance R with V_{tg} and V_{bg} on a
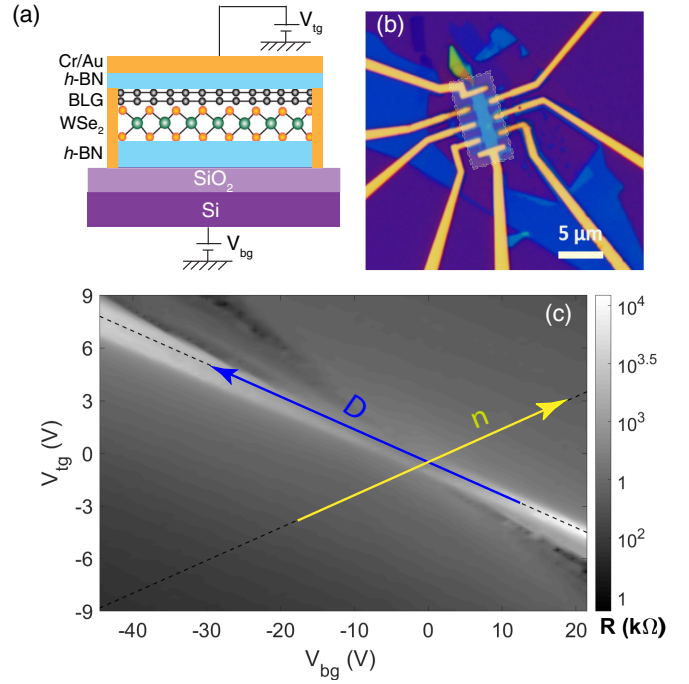

FIG. 1. (a) Schematic of the device structure. The BLG and single-layer WSe$_2$ stack is sandwiched between two h-BN flakes of thickness ~20 nm. (b) Optical image of the device without top-gate structure—the gray rectangle shows the position of the top gate. (c) Contour plot of four-probe resistance measured in the V_{bg}-V_{tg} plane on logarithmic scale. The blue and yellow arrows indicate the directions of increasing D and n, respectively.

logarithmic scale. The blue and yellow arrows indicate the directions of increasing D and n, respectively. A contour plot of the logarithm of the four-probe longitudinal resistance R as functions of n and D [Fig. 2(a)] shows that the resistance at the Dirac point increases with an increase in $|D|$ establishing the opening of a band gap in BLG. Along with the prominent peak at Dirac point, an asymmetric feature is observed near it as outlined by the yellow dashed curve in Fig. 2(a). This is a direct consequence of the predicted spin splitting of the VB and CB due to proximity-induced SOI in BLG [11] and observed recently through penetration field capacitance studies [17] and transport measurements [26]. This asymmetric feature in the n-D plane depends on the direction and magnitude of displacement field—appearing in the positive (negative) n regime for positive (negative) D [Fig. 2(b)].

These observations can be understood by noting that the presence of the single-layer WSe$_2$ causes the BLG to experience, in addition to the strong valley Zeeman SOI, a displacement field of the order of -0.25 V/nm making it layer polarized. For $D < 0$, the Bloch waves associated with the VB and CB of the BLG reside on the bottom layer and top layer, respectively [Fig. 3(a)]. Since the bottom layer is in close contact with the WSe$_2$, the VB is prominently spin split. This splitting increases as D is made more negative via the gate voltages. Upon changing
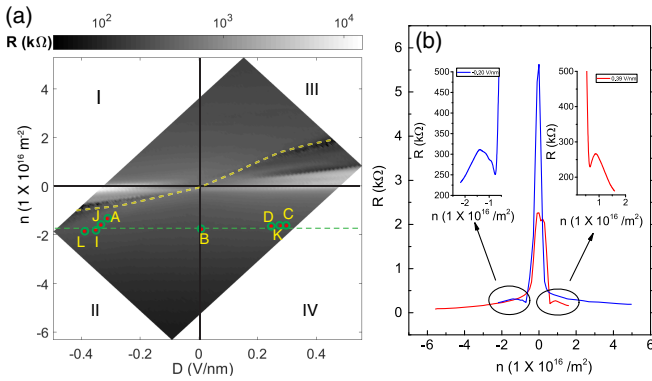
FIG. 2. (a) A two-dimensional contour plot of R as a function of n and D. The asymmetric feature around the primary Dirac point (marked by the dashed line) is a consequence of the fact that only one of the bands (VB for negative D and CB for positive D) gets split due to induced SOI [11]. The data were acquired at $T = 20$ mK and $B = 0$ T. The labels I–IV mark the four quadrants in the n-D plane. The corresponding regimes are marked in the two schematic band structures in Fig. 3. The weak localization or weak antilocalization measurements reported in this Letter were performed along the green line (some of the points are labeled). (b) Plots of R versus n for $D = -0.2$ V/nm (blue line) and $D = 0.4$ V/nm (red line). The insets show the data enlarged around the secondary peaks (marked in the main panel by dashed ovals) arising from SOI-induced splitting of the bands.

D to increasingly positive, the band gap initially closes as the external field cancels out that due to the WSe_2. On increasing D further, the band gap reopens, but now the layer polarization of the BLG reverses direction, causing the lower layer to form the spin-split CB [Fig. 3(b)]. Calculations show that this will cause the system to undergo a displacement field induced topological phase transition into the anomalous valley Hall phase [12] and quantum spin Hall phase [26] as recently demonstrated.

Having established displacement field induced band inversion in our device, we move on to probe the electron dynamics as we transit from the trivial VB at $D > 0$ to the nontrivial spin-split VB at $D < 0$. The SOI mechanism can be effectively probed by studying the quantum correction to the conductance in the presence of a perpendicular magnetic field B. The magnetoconductance measurements were performed in the parameter space of D-n plane along the green line shown in Fig. 2(a) for a $n = -1.8(\pm 0.05) \times 10^{16}$ m^{-2} while changing $|D|$ from negative to positive. To avoid contamination of the data by universal conductance fluctuation [34], each plot is an ensemble average of 40 traces measured at very close values of n (spanning the range $\Delta n = \pm 0.05 \times 10^{16}$ m^{-2}).

The four-terminal magnetoconductance $\Delta\sigma(B) = \sigma(B) - \sigma(0)$ traces plotted in Fig. 4(a) show a clear crossover from WAL to WL as the displacement field changes from negative to positive. This transition can be understood as follows: for negative D and chemical potential E_F lying in VB (regime II in Figs. 2 and 3),
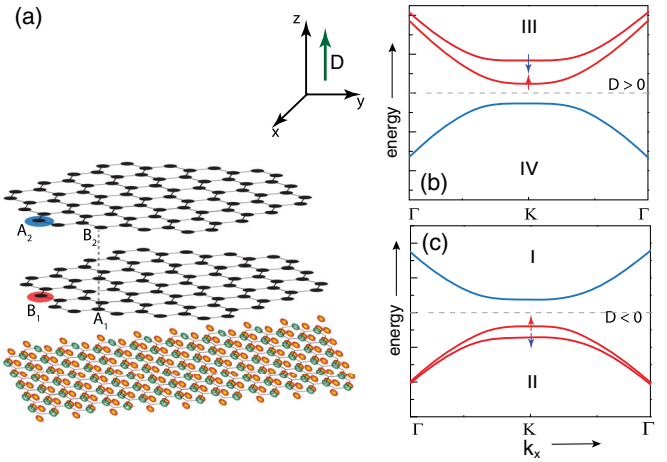

FIG. 3. (a) Schematic showing the single-layer WSe_2 and the two layers of the BLG. The low-energy bands in the BLG arise from hopping between the orbitals on the nondimer pair of sites formed of B_1 sublattice of the lower layer (one such atom is marked in red) and the A_2 sublattice of the top layer (one such atom is marked in blue) [33]. The system lies in the x-y plane, while the positive direction of D (indicated by the green arrow) is the positive z axis. (b) Schematic of the bulk band structure near the K valley for positive values of D. The electrons localized in the bottom layer (B_1 orbital) of the BLG form the spin-split CB, and those in the top layer (A_2 orbital) of the BLG form the VB [11]. (c) Schematic of the bulk band structure plotted near the K valley for negative D. The electrons localized in the B_1 orbital of the BLG now form the spin-split VB, and those in the A_2 orbital of the BLG form the CB. The BLG thus undergoes a band inversion as D changes sign [11].

the holes experience a strong SOI. This, along with the breaking of the $z \to -z$ symmetry, leads to the observed WAL [27]. As the displacement field becomes positive, the electrons in conduction bands experience strong SOI, while the SOI in VB reduces to a value intrinsic to BLG, which, as discussed before, is extremely small. Since the E_F still lies in the VB (regime IV in Figs. 2 and 3), we observe WL, which is the characteristic of BLG due to its intrinsic Berry phase of 2π. This transformation of the magnetoconductance from WAL to WL again demonstrates displacement field induced band inversion in BLG/WSe_2 heterostructures. Figure 4(a) also shows the magnetoconductance for $D \sim 0.01$ V/nm (blue data points). In this crossover regime, the orbitals localized in both the upper and the lower layer of the BLG contribute equally to the valance and conduction bands leading to a magnetoconductance curve, which is a complex admixture of WL (arising from the intrinsic Berry curvature of unbiased BLG) and WAL (due to the induced SOI).

As mentioned earlier, the McCann-Fal'ko equation cannot be used to extract the scattering timescales in our system, as it does not take into account the spin splitting of bands. To get a quantitative estimate of different scattering timescales involved, the magnetoconductance data were
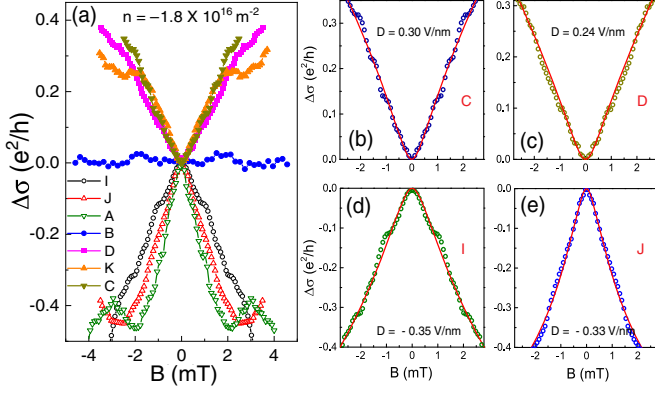
FIG. 4. (a) Plots showing the dependence of the ensemble averaged magnetoconductance data on B for $n = -1.8 \times 10^{16}$ m^{-2} at different D. The data were collected along the green dotted line in Fig. 2. For $D < 0$, WAL is observed which changes to WL as the D is made sufficiently positive. The blue data points (measured at point B in Fig. 2) show the magnetoconductance near $D \sim 0.01$ V/nm. (b),(c) The open circles are the ensemble averaged WL data taken for $D > 0$ and $n < 0$ (regime IV in Figs. 2 and 3). The solid red lines are the fits to the data using Eq. (1). (d),(e) The open circles are the ensemble averaged WAL data taken for $D < 0$ and $n < 0$ (regime II in Figs. 2 and 3). The solid red lines are the fits to the data using Eq. (2). The letters C, D, I, and J refer to the points in the n-D plane in Fig. 2 at which the data were collected.

analyzed following the approach recently [24] which discusses the two different regimes taking into account the relative strengths of the SOI interaction Δ_{so} [20] and intervalley scattering rate τ_{iv}^{-1}. The valley Zeeman SOI is a strong source of symmetric spin relaxation rate [20,35]. In the presence of this component of SOI, the net symmetric spin relaxation rate becomes $\tau_{sym}^{-1} \rightarrow \tau_{sym}^{-1} + 2\Delta_{so}^2 \tau_{iv}$. The asymmetric spin relaxation rate τ_{asy}^{-1}, on the other hand, arises from the Rashba SOI. When E_F lies in VB and the CB is spin split ($D > 0$), this regime is characterized by $\tau_{iv}^{-1} > \Delta_{so}$. In this WL regime, for phase coherence rate τ_ϕ^{-1} comparable to τ_{iv}^{-1}, the magnetoconductance can be analyzed using the following equation [24]:

$$\Delta\sigma(B) = \frac{e^2}{\pi h}\left[F\left(\frac{B}{B_\phi}\right) - F\left(\frac{B}{B_\phi + 2B_{iv}}\right) + 2F\left(\frac{B}{B_\phi + B_{iv}}\right)\right],$$

(1)

where $F(z) = \ln(z) + \psi[\frac{1}{2} + (1/z)]$, ψ is the digamma function, $B_i = \hbar/(4e\tilde{D}\tau_i)$, and $\tilde{D}$ is the diffusion coefficient [36]. For $D < 0$, and E_F lying in the spin-split VB, the system is characterized by $\Delta_{so} > \tau_{iv}^{-1}$. Because of strong valley Zeeman SOI, WL gets suppressed, and one will observe WAL described by the following equation [24]:

$$\Delta\sigma(B) = \frac{e^2}{2\pi h}\left[F\left(\frac{B}{B_\phi + 2B_{asy}}\right) - F\left(\frac{B}{B_\phi}\right)\right],$$

(2)

where B_{asy} corresponds to the scattering rate τ_{asy}^{-1}. Physically τ_{asy}^{-1} corresponds to the spin-flip processes that break the $z \rightarrow -z$ symmetry induced by Rashba SOI.

Figures 4(b) and 4(c) are plots of WL and the data were fitted using Eq. (1). The WAL data are shown in Figs. 4(d) and 4(e) and have been fitted using Eq. (2). The extracted timescales are tabulated in Supplemental Material [31]. In the case of WAL, τ_{asy} was found to be $\sim$0.5–2 ps, smaller than τ_ϕ, which varies between 7 and 22 ps, consistent with the earlier observations [18,21] and theoretical predictions [23]. For the WL case, τ_{iv} (0.9–2 ps) was found to be smaller than τ_ϕ (9–14 ps). The above analysis establishes that electron interference effects are dominated by spin-flip processes in the spin-split band and by intervalley scattering in the spin-degenerate bands of BLG. It also shows that the strength of the SOI can be tuned from a significant value to negligibly small by the external electric field—this unequivocally establishes the realization of the spin-orbit valve effect and is one of the central results of this Letter [11].

Additional support to our claim of electric-field-tuned band inversion and SOI-induced band splitting comes from the results of Shubnikov–de Haas (SdH) oscillations measurements. The data were collected in a similar device of higher mobility ($\sim$100, 000 cm^2 V^{-1} s^{-1}) at a constant number density $n \sim 3 \times 10^{16}$ m^{-2}. Each measurement consisted of $\sim$3000 data points and was performed for several values of D between -0.15 and 0.15 V/nm. For $n > 0$ and $D > 0$ (regime III) we observe a beating pattern in the SdH oscillations; Fig. 5(b) shows representative data for $D = 0.15$ V/nm. The beating results from the presence of two close-by frequencies of nearly equal magnitudes in
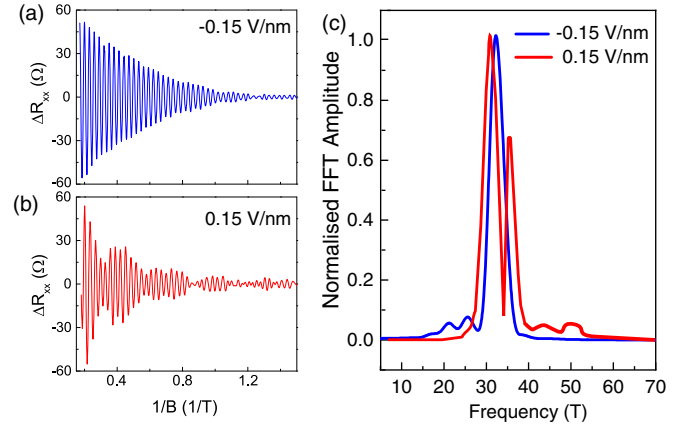

FIG. 5. Shubnikov–de Haas oscillations (measured at $n \sim 3 \times 10^{16}$ m^{-2}) plotted versus $1/B$ for (a) $D \sim -0.15$ V/nm and (b) $D \sim 0.15$ V/nm. The beating in the oscillations observed for positive values of D indicates the presence of two close-by frequencies. (c) The red and blue curves show, respectively, the Fourier transform of the SdH oscillations for $D \sim 0.15$ V/nm and $D \sim -0.15$ V/nm. One can see a clear change in the Fermi surface topology from single (regime I in Figs. 2 and 3) to doubly split (regime III in Figs. 2 and 3) on changing D from negative to positive.

the signal. The FFT data plotted in Fig. 5(c) confirm the presence of two frequencies at ~31.5 and ~36.1 T reflecting the presence of two extrema of the Fermi surface at this energy. This SOI-induced band splitting has been reported previously in BLG/WSe$_2$ heterostructures [18]—although in that case, a study of displacement field tunability was lacking. When the experiment was repeated for $D < 0$ (regime I), no beating pattern was observed [see Fig. 5(a) for data at $D = -0.15$ V/nm]—the FFT of the data has a single peak at ~32.6 T [Fig. 5(c)]. Thus, a clear transition from a single Fermi surface to two Fermi surfaces is observed as D is varied from negative (regime I) to positive (regime III) when E_F lies in the CB. The results of SdH oscillations complement our observation, from low-field magnetoresistance measurements, of transition from a single Fermi surface to two Fermi surfaces as D is varied from positive (regime IV) to negative (regime II) for E_F lying in the VB. We thus demonstrate "on-demand" electric-field-induced band-structure modulation of BLG over all four regimes marked in Fig. 2(a).

In summary, we demonstrate an electric-field-induced band-structure engineering in BLG. Through magnetotransport measurements, we observe a transition from a topologically trivial to a nontrivial band in BLG. The low-energy carriers in the BLG experience an effective valley Zeeman SOI that is gate tunable to the extent that it can be switched on or off by applying a transverse displacement field or can be controllably transferred between the valence and the conduction band. This leads to the realization of the predicted spin-orbit valve effect.

---

[*]aveek@iisc.ac.in

[1] Y. Liu, N. O. Weiss, X. Duan, H.-C. Cheng, Y. Huang, and X. Duan, Nat. Rev. Mater. **1**, 16042 (2016).

[2] A. K. Geim and I. V. Grigorieva, Nature (London) **499**, 419 (2013).

[3] B. V. Lotsch, Annu. Rev. Mater. Res. **45**, 85 (2015).

[4] H. Wang, F. Liu, W. Fu, Z. Fang, W. Zhou, and Z. Liu, Nanoscale **6**, 12250 (2014).

[5] X. Zhou, X. Hu, J. Yu, S. Liu, Z. Shu, Q. Zhang, H. Li, Y. Ma, H. Xu, and T. Zhai, Adv. Funct. Mater. **28**, 1706587 (2018).

[6] K. S. Novoselov, A. Mishchenko, A. Carvalho, and A. H. C. Neto, Science **353**, aac9439 (2016).

[7] C. Kumar, S. K. Srivastav, P. Adhikary, S. Banerjee, T. Das, and A. Das, Phys. Rev. B **98**, 155408 (2018).

[8] M. Gmitra, S. Konschuh, C. Ertler, C. Ambrosch-Draxl, and J. Fabian, Phys. Rev. B **80**, 235431 (2009).

[9] C. Weeks, J. Hu, J. Alicea, M. Franz, and R. Wu, Phys. Rev. X **1**, 021001 (2011).

[10] K. Hatsuda, H. Mine, T. Nakamura, J. Li, R. Wu, S. Katsumoto, and J. Haruyama, Sci. Adv. **4**, eaau6915 (2018).

[11] M. Gmitra and J. Fabian, Phys. Rev. Lett. **119**, 146401 (2017).

[12] J. Y. Khoo, A. F. Morpurgo, and L. Levitov, Nano Lett. **17**, 7003 (2017).

[13] A. W. Cummings, J. H. Garcia, J. Fabian, and S. Roche, Phys. Rev. Lett. **119**, 206601 (2017).

[14] M. Gmitra and J. Fabian, Phys. Rev. B **92**, 155403 (2015).

[15] M. Offidani, M. Milletarì, R. Raimondi, and A. Ferreira, Phys. Rev. Lett. **119**, 196801 (2017).

[16] J. C. Leutenantsmeyer, J. Ingla-Aynés, J. Fabian, and B. J. van Wees, Phys. Rev. Lett. **121**, 127702 (2018).

[17] J. Island, X. Cui, C. Lewandowski, J. Khoo, E. Spanton, H. Zhou, D. Rhodes, J. Hone, T. Taniguchi, K. Watanabe et al., Nature (London) **571**, 85 (2019).

[18] Z. Wang, D.-K. Ki, J. Y. Khoo, D. Mauro, H. Berger, L. S. Levitov, and A. F. Morpurgo, Phys. Rev. X **6**, 041020 (2016).

[19] L. A. Benítez, J. F. Sierra, W. Savero Torres, A. Arrighi, F. Bonell, M. V. Costache, and S. O. Valenzuela, Nat. Phys. **14**, 303 (2018).

[20] S. Zihlmann, A. W. Cummings, J. H. Garcia, M. Kedves, K. Watanabe, T. Taniguchi, C. Schönenberger, and P. Makk, Phys. Rev. B **97**, 075434 (2018).

[21] S. Omar and B. J. van Wees, Phys. Rev. B **97**, 045414 (2018).

[22] J. Xu, T. Zhu, Y. K. Luo, Y.-M. Lu, and R. K. Kawakami, Phys. Rev. Lett. **121**, 127703 (2018).

[23] J. H. Garcia, M. Vila, A. W. Cummings, and S. Roche, Chem. Soc. Rev. **47**, 3359 (2018).

[24] S. Ilić, J. S. Meyer, and M. Houzet, Phys. Rev. B **99**, 205407 (2019).

[25] Z. Wang, D.-K. Ki, H. Chen, H. Berger, A. H. MacDonald, and A. F. Morpurgo, Nat. Commun. **6**, 8339 (2015).

[26] P. Tiwari, S. K. Srivastav, S. Ray, T. Das, and A. Bid, ACS Nano **15**, 916 (2021).

[27] E. McCann and V. I. Fal'ko, Phys. Rev. Lett. **108**, 166606 (2012).

[28] H. Ochoa, F. Finocchiaro, F. Guinea, and V. I. Fal'ko, Phys. Rev. B **90**, 235429 (2014).

[29] F. Pizzocchero, L. Gammelgaard, B. S. Jessen, J. M. Caridad, L. Wang, J. Hone, P. Bøggild, and T. J. Booth, Nat. Commun. **7**, 11894 (2016).

[30] L. Wang, I. Meric, P. Huang, Q. Gao, Y. Gao, H. Tran, T. Taniguchi, K. Watanabe, L. Campos, D. Muller et al., Science **342**, 614 (2013).

[31] See Supplemental Material at http://link.aps.org/supplemental/10.1103/PhysRevLett.126.096801 for additional raw data, detailed discussion on device fabrication, measurement techniques and analysis, which includes Ref. [32].

[32] Y. Zhang, T.-T. Tang, C. Girit, Z. Hao, M. C. Martin, A. Zettl, M. F. Crommie, Y. R. Shen, and F. Wang, Nature (London) **459**, 820 (2009).

[33] E. McCann and M. Koshino, Rep. Prog. Phys. **76**, 056503 (2013).

[34] P. A. Lee and A. D. Stone, Phys. Rev. Lett. **55**, 1622 (1985).

[35] J. H. Garcia, M. Vila, A. W. Cummings, and S. Roche, Chem. Soc. Rev. **47**, 3359 (2018).

[36] R. V. Gorbachev, F. V. Tikhonenko, A. S. Mayorov, D. W. Horsell, and A. K. Savchenko, Phys. Rev. Lett. **98**, 176805 (2007).